JOURNAL OF AIRCRAFT
Vol. 45, No. 3, May–June 2008

Wind-Tunnel Testing and Modeling of a Micro Air Vehicle with Flexible Wings

R. Albertani* and B. Stanford†
University of Florida, Gainesville, Florida 32611
R. DeLoach‡
NASA Langley Research Center, Hampton, Virginia, 23681
J. P. Hubner§
University of Alabama, Tuscaloosa, Alabama 35487
and
P. Ifju¶
University of Florida, Gainesville, Florida 32611

DOI: 10.2514/1.33338

The field of micro air vehicles is relatively immature; consequently, high-fidelity simulations do not yet exist for a generic aircraft. The fidelity of flight dynamic simulations is closely correlated to the reliability of models representing the vehicle's aerodynamic and propulsion characteristics in the entire flight envelope, including the nonlinear region. This paper discusses wind-tunnel experiments performed to investigate the aerodynamic and mechanical characteristics of micro air vehicles with flexible wings in different conditions of propeller type, motor power, and elevator deflections. Visual image correlation was used to measure the deformation of the flexible wings to quantify general features such as variations in aerodynamic and geometric twist angle. Aerodynamic and propulsion results were used to formulate empirical models of the relevant coefficients in the form of multiple linear regressions and to estimate the effectors' functional dependencies and interactions. High-order nonlinear interactions were confirmed between the coefficients of lift, drag, and pitching moment with the independent variables. The rates of the dependencies with elevator deflections and angle of attack were found, to some extent, to be motor voltage and dynamic pressure dependent, evincing a strong coupling with the propeller speed.

Nomenclature

a_i	=	response surface coefficients
C_D	=	coefficient of drag
C_L	=	coefficient of lift
C_m	=	coefficient of pitching moment measured at 25% of the root chord
E	=	motor voltage, V
m	=	number of terms in the response surface
N	=	number of experiments
n	=	propeller speed, krpm (kilo rounds per minute)
q	=	dynamic pressure, Pa
R	=	asymmetry ratio
R_2	=	coefficient of determination
U_∞	=	freestream velocity, m/s
w	=	out-of-plane displacement, mm
x, y, z	=	Cartesian displacement directions
α	=	angle of attack, deg
δ	=	elevator deflection, deg
σ_0^2	=	variation

Received 9 July 2007; revision received 26 October 2007; accepted for publication 23 November 2007.

*Research Assistant Professor, Research and Engineering Education Facility, Shalimar, FL. Member AIAA.
†Graduate Research Assistant, Mechanical and Aerospace Engineering. Member AIAA.
‡Senior Research Scientist. Senior Member AIAA.
§Assistant Professor, Aerospace and Mechanical Engineering. Associate Fellow AIAA.
¶Professor, Mechanical and Aerospace Engineering.

I. Introduction

THE general morphological features of micro air vehicles (MAVs) are a maximum linear dimension of 15 cm, 50 g mass, and flying speeds between 10 and 15 m/s. The compact design requirements make the use of a low aspect ratio (LAR) flying wing the preferred configuration, as illustrated in Fig. 1. A typical mission for a MAV is surveillance, with particular interest to urban areas. Such a profile requires highly agile maneuverability while maintaining benign flying characteristics in the entire flight envelope to prevent expanding the pilot or the autonomous flight control system beyond its capability. A high-fidelity simulation model representing the vehicle's aerodynamic and propulsion characteristics (in both the linear and nonlinear regions of the flight envelope), when integrated with the control and dynamic derivative terms, could be used to help meet the above constraint. Such a simulation model could also be used to conduct performance analysis, stability and control assessment, energy balance for battery life optimization, and mission planning.

Numerical studies by Lian and Shyy [1] and Viieru et al. [2] have investigated the aerodynamic characteristics of flexible-wing MAVs, including the fluid-structure interactions demonstrating the benign effects of a flexible wing with respect to a rigid configuration. Experimental aerodynamic studies were carried out by Torres [3] and Pellettier and Mueller [4] on rigid LAR wings for MAV applications, presenting relevant results on the aerodynamics at low Reynolds numbers. The fundamental aerodynamics of flexible wings and elastic deformation shapes were experimentally measured by Waszak et al. [5] and later by Albertani et al. [6,7] to demonstrate the link between aerodynamic characteristics and the MAV wing's structural flexibility. Waszak et al. [8] used polynomial expressions to describe the main aerodynamic and propulsion coefficients measured from wind-tunnel tests and develop a simulation of the vehicle's flight control. The above work set a baseline for MAV control system modeling but did not offer insights into the experimental variables and their mutual interactions.

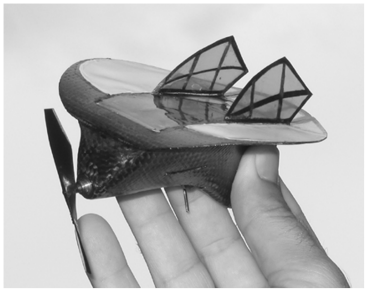

Fig. 1 MAV equipped with a low aspect ratio membrane wing.

This paper describes the experimental procedures and results applied toward the development of a wind-tunnel database on powered MAVs with variable flexible wings, including the effects of the propeller on the aerodynamic characteristics and the coupling with elevator control. Fundamental work on wind-tunnel experiments and modeling from experimental data was described by Morelli [9] and DeLoach [10], unequivocally demonstrating the substantial value of modern design of experiments (MDOE) applied to wind-tunnel experiments and the general testing of a powered aircraft model. The model structure identification suggested by Morelli [9] was partially applied to the present work, and a portion of the data analysis is inspired by MDOE postprocessing techniques.

II. Experimental Setup

The shape of the flexible wings employed in the current work passively adapts to the test conditions: the aerodynamics cannot be fully explained without characterizing the wing structures. Two main experimental arrangements were applied for this research: 1) a strain gage six-component sting balance for force and moment measurements and 2) a visual image correlation (VIC) system, to measure the elastic structural deformation along the flexible MAV wing.

A. Vehicle Description

The MAVs used in the wind-tunnel testing consisted of flight ready vehicles without the payload and batteries. All vehicles shared the same fuselage, vertical stabilizer, and control components. The wing area is $1.78\text{E}-02\ \text{m}^2$, the root chord is 130 mm, the camber at the root is 3.50 mm, the wingspan is 150 mm, and the wing's aspect ratio is 1.26. The three geometrically identical wings were built from a combination of thin carbon fiber and latex skin (Fig. 2). The nominally rigid wing was made from three plies of bidirectional carbon fiber oriented at 45 deg to the aircraft's longitudinal axis and used as a reference for the aerodynamic characteristics. The flexible-wing structures were manufactured from two plies of bidirectional carbon fiber; the batten reinforced (BR) wing has battens made from two unidirectional plies reinforcing the latex membrane, while the perimeter reinforced (PR) wing has no battens but the carbon fiber extends around the entire wing (Fig. 2). The former provides a certain measure of passive adaptive geometric twist, as the trailing edge is free to deform due to the aerodynamic loading. The latter membrane structure provides an adaptive aerodynamic twist: both the leading and trailing edges of each membrane wing section are attached to relatively stiff carbon fiber reinforcement. Wing loading inflates the membrane skin, adaptively increasing the camber.

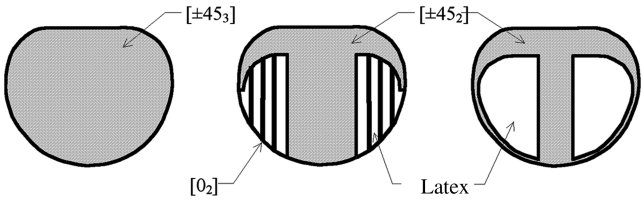

Fig. 2 Three distinct MAV wing structures, from left to right: the rigid wing (R), the batten reinforced wing (BR), and the perimeter reinforced wing (PR).

The electric motor used for all tests was a dc Maxon RE-10 and the propeller a U80 with a nominal diameter of 80 mm and a pitch of 50 mm. Flight tests on the same vehicles have indicated that the optimum U80 propeller diameter is 58 mm; therefore the standard wind-tunnel tests were performed using this reduced size propeller. All of the models were equipped with servo actuators for tests with control deflections; the actuators were not energized and the desired angle was set manually for each experiment using templates.

B. Wind Tunnel

All tests were conducted in an open-circuit, low-speed, low turbulence wind tunnel with a $0.9 \times 0.9 \times 2.0$ m test section and a maximum flow velocity of 16.0 m/s. Typical testing Reynolds numbers, based on wing chord geometry, range between 50,000 and 150,000. The aerodynamic forces and moments were acquired through a six-component sting balance with a resolution is 0.03 N. The calibration of the sting balance was performed within the specific range of the aerodynamic forces predicted during the tests and an error analysis was conducted [11]. A typical installation of the MAV in the wind tunnel is illustrated in Fig. 3.

C. Wing Structural Deformation Measurements

The models' off-wind (undeformed) geometry and the subsequent full-field displacement were obtained using a VIC system during wind-tunnel tests. To capture the three-dimensional geometry of the models, synchronized twin cameras, each pointing from a different viewing angle, were installed over the wind-tunnel ceiling. The operational principle of the VIC [12] is to determine the displacements of the specimen under load by tracking the deformation of a subset of a random speckling pattern applied to the surface [6]. Displacement data are obtained relative to a reference condition, typically wind-off or power-off conditions. The VIC is able to attain subpixel resolution: the resolution of the system was experimentally estimated to be on the order of 0.05 mm.

D. Test Procedure

The procedure for the experiments illustrated in this paper followed a traditional one factor at a time (OFAT) technique. Power sweeps at constant angle of attack and velocity (including wind off) were performed followed by classical α sweeps at random extreme motor settings, freestream velocities, and elevator settings to define the range of the independent variables and to identify relevant subspaces for modeling. The response variables were the propeller speed, the motor current consumption, and the aerodynamic coefficients. The subspaces of the four independent variables were identified as follows: 1) angle of attack (two ranges of 4–18 deg and 18–36 deg were selected); 2) motor voltage (no power, 6.6, 7.0, and 7.4 V); 3) elevator angle (between -30 and $+30$ deg); and 4) freestream velocity (four discrete levels of 8.0, 10.0, 11.5, and 13.0 m/s).

VIC was used to acquire the wing's 3-D geometry and deformation field for selected points in the test matrix at specified angles of attack, freestream velocity, and motor setting. The experiments consisted of three steps for each data point, as follows:

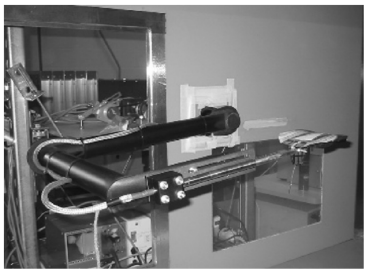

Fig. 3 The MAV installed in the wind tunnel: the vehicle is connected to an external balance via a variable angle-of-attack model arm.

1) A reference image was taken of the wing's shape in wind-off and power-off conditions.

2) A second image was taken of the wing deformed due to freestream only (wind-on/power-off conditions).

3) A third image was taken of the wing deformed due to both freestream and propeller downwash (wind-on/power-on conditions).

Both the second and the third images were processed through the VIC system, using the first as a reference image to calculate the respective displacement fields along the flexible wings.

III. Modeling Procedure

The typical task of modeling consists of finding the correct functional dependencies of the output variables on the independent variables using polynomial relationships. Various modeling techniques can be used according to the number of independent variables, their range, and the level of intrinsic complexity of the functional dependency. For the proposed work the number of independent variables is relatively small and the results contain mild nonlinearities characterized by noncomplex dependencies. Therefore, the authors have chosen to apply a least-squares linear regression technique coupled with the predicted squared error (PSE) and the mean squared error (MSE) [10,13]. The regression analysis was performed using a Maclaurin-type expansion with linear coefficients and a combination of linear and nonlinear functions.

The MSE gives a merit for the model's fit to the data. Repetition tests give the perception of how future input data will be dispersed with an estimate of the variance of a large population of dependent variables. Assuming that training input data can be chosen or generated to be representative of future data, the PSE simplifies to

$$\mathrm{PSE} = \mathrm{MSE} + 2\sigma_0^2(m/N) \tag{1}$$

The optimum model structure corresponds to the global minimum of the PSE function. The second technique used a standard procedure [14] to determine the response surfaces. A factorial design was also used to test the capability of improving the efficiency of the experiments in terms of a required number of data points and interactions detected. The following results will demonstrate the functional models, highlighting several interactions between independent variables and their effect on the response variables.

IV. Tests Results and Discussion

A. Structural Elastic Deformations Results

The primary results obtained from the structural tests consist of the discrete geometry of the wing surface in x, y, and z coordinates at the different test conditions. The reference state for the displacements was typically wind off or power off at the desired angle of attack. When the wing's deformed shape is known it is possible to compute the plane-strain field [6] and the relevant geometric characteristics such as camber, camber position, and wing twist [7]. The plane-strain field is defined by the three strains ε_{xx}, ε_{yy}, and ε_{xy} acting parallel to the wing's surface. The wing's thin membrane is characterized by a plane-stress state in which the two-dimensional stress tensor generates a three-dimensional strain tensor. The nonzero out-of-plane strain component evolves from the Poisson's effect, which has no relevance for the current scope and was not measured. The displacement field along a specific MAV wing can be considered a variable of three factors: the flow's dynamic pressure, the wing's angle of attack, and the propeller operating conditions (if applicable) via its slipstream. The maximum displacement found within a flexible MAV wing will increase with higher flow speeds and, up to a certain level (typically wing stall), with higher angle of attack. In addition, the absence of any propeller will lead to a displacement field that is reasonably symmetric about the root of the MAV [6,7].

Experimental verification of the different behavior of the two membrane wing designs is given in Figs. 4 and 5, depicting the contour plots of the out-of-plane displacement field of a BR and a PR wing, respectively. The results were taken at an angle of attack of 4 deg and a flow velocity of 8 m/s; the plots on the left of each figure

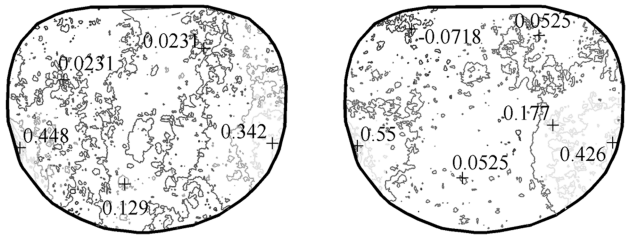

Fig. 4 Out-of-plane displacements (mm) of a batten reinforced (BR) wing at $\alpha = 4$ deg and $U_\infty = 8$ m/s: propeller in windmill (left), and with power (right).

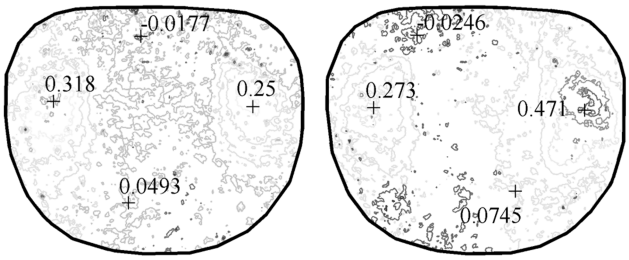

Fig. 5 Out-of-plane displacements (mm) of a perimeter reinforced (PR) wing at $\alpha = 4$ deg and $U_\infty = 8$ m/s: propeller in windmill (left), and with power (right).

are with the propeller in windmill conditions (power off) and on the right with the motor setting at 7.4 V. The propeller used for these tests was the original U80 with a nominal diameter of 80 mm, resulting in a vehicle wingspan-propeller diameter ratio of 1.88. The propeller speeds in windmill and powered conditions were 7750 and 18,300 rpm, respectively. The adaptive washout of the BR, evinced by the higher positive deformation areas close to the wing tips and trailing edge, is illustrated in Fig. 4. The nose-down twist of the flexible-wing sections was found, through flight testing, to improve the stall angle of the wing and provide a certain measure of gust rejection [15]. Maintaining control of a MAV in gusty conditions can be particularly challenging, as the disturbance may be of the same magnitude as the original flight speed. A slight asymmetry in the BR wing's deformation field can be seen when the propeller is in windmill, an effect which is obviously exacerbated when power is applied. The left side of the wing is generally unaffected, while the right side experiences a sharper nose-down twist.

The adaptive aerodynamic twist of the PR wing can be seen in Fig. 5. This passive membrane inflation increases the camber of the wing and shifts the camber aftward. Wind-tunnel testing has shown that such a membrane structure increases the lift and the longitudinal static stability, as compared to a rigid wing [6]. The latter represents a main target of design improvement from a generation of MAVs to the next, as the range of stable flight center of gravity locations on a MAV is typically only a few millimeters long. The asymmetry of the membrane wing's shape due to a powered propeller is substantial and is identified from the numerical values on the contour plots in Figs. 4 and 5. The right wing is more affected, resulting in a larger aerodynamic twist.

An effective quantitative assessment of a propeller's slipstream wash effects on the wing deformation is proposed as follows. The ratio R is defined as the ratio of the integrals of the out of-plane displacements (w) of the two semiwings according to the following equation:

$$R = \frac{\int_A w(x,y)\,\mathrm{d}A|_{\mathrm{left}}}{\int_A w(x,y)\,\mathrm{d}A|_{\mathrm{right}}} \tag{2}$$

Steady flow conditions in the absence of a propeller should yield a ratio R of unity. For a completely rigid wing, the ratio would potentially tend toward the indeterminate value of $0/0$, and the experimentally measured R would become very noisy and erratic. Such a problem is prevented by rigid body motions inherent within

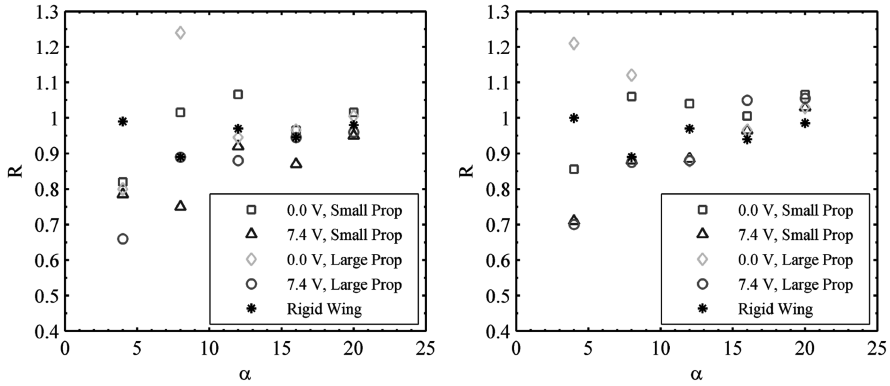

Fig. 6 Displacement asymmetry ratio at $U_\infty = 8$ m/s: batten reinforced wing (left), and perimeter reinforced wing (right).

the wind-tunnel setup (the flexibility of the strain gage sting balance slightly increases the angle of attack of the entire wing, as can be seen in the nonzero displacements measured from the rigid root of the BR and PR wings in Figs. 4 and 5). These rigid body motion terms would be included in both the numerator and the denominator, and the ratio should tend toward unity even for a rigid wing. Indeed, tests performed on the rigid wing resulted in an average ratio R of 0.956, considered as indicative of the uncertainty value in the results. The difference of the ratio from unity gives a reasonable indication of the asymmetry of the wing and thus suggests a quantitative evaluation of the propeller slipstream wash. Physically, each integral represents the volume bounded between the deformed and the reference wing surface. With the knowledge that the VIC system produces a discrete scheme with equal grid spacing (on the order of 0.5 mm) in both the x and y directions, this ratio can be fairly well approximated through the following numerical integration:

$$R \approx \frac{\sum_{i=1}^{N} w_i|_{\text{left}}}{\sum_{i=1}^{N} w_i|_{\text{right}}} \tag{3}$$

The computed ratios for the BR wing and the PR wing are depicted in Fig. 6 at 8 m/s, for both windmilling and powered propeller at 7.4 V. Despite some noise in the data gathered with the large propeller (80 mm) in windmilling conditions, the proposed ratio appears to perform as intended. Ratios on the order of 0.6 (indicating a substantial wing asymmetry) were detected for low angles of attack and relatively high motor power. Data at higher angles of attack approach unity, due to the overwhelming effects of the (symmetric) freestream dynamic pressure over the propeller wake. As the asymmetric wing shapes are more pronounced for the PR wings (Fig. 5) than the BR wings (Fig. 4), so the convergence of the ratio toward unity with increased angle of attack is generally cleaner for the PR wing, with less scatter in the data. The values of the ratio for the rigid wing are also reported for comparison: as expected, the data are scattered about unity, with no obvious relationship to angle of attack.

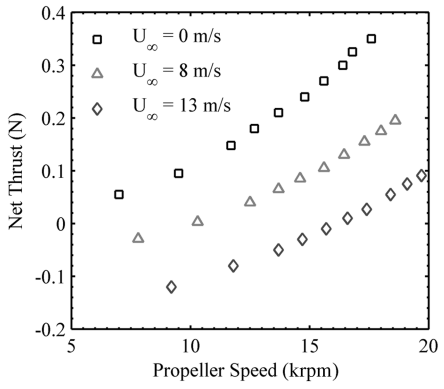

Fig. 7 Power sweeps at $\alpha = 4$ deg.

B. Propulsion Parameters

A general assessment of the propulsion characteristics was obtained from power sweeps at different wind-tunnel flow velocities, including a wind-off condition using a generic rigid wing configuration. The results illustrated in Fig. 7 were gathered at $\alpha = 4$ deg and represent the net thrust obtained from algebraic summation of the power-on forces and propeller-off vehicle aerodynamics. The difference in net thrust at different freestream velocities is evident from the figure. The propeller speed was measured and a fit function was derived in the entire range of angles of attack, up to 38 deg. Using the procedure described in Sec. III, the best function to estimate the propeller speed (in krpm) was found to be

$$n = a_0 + a_1 q + a_2 \alpha + a_3 \alpha^2 + a_4 E + a_5 \alpha E + a_6 \alpha q + a_7 q E + a_8 E^2 \tag{4}$$

The values of the constant model parameters are reported in Tables 1 and 2. The function for propeller speed contains a linear term with dynamic pressure and nonlinear terms with voltage motor input and α, accounting for the nonlinear dependence on those terms observed in the tests. The presence of the αE, αq, and qE cross terms was attributed to the motor-propeller system performance dependency on the freestream velocity and is thought to be a result of the wing's upwash effect on propeller speed observed during the tests and in previous works [5,16].

C. Aerodynamic Coefficients Without Propeller

The series of wind-tunnel tests were performed on the MAVs without a propeller, including the BR, PR, and the rigid wing as a reference. Repetition tests were used for assessing the quality of the tests and the general merit of the fit functions. A relevant characteristic found in the data was a significant block effect, attributed to across-run differences in freestream velocity, temperature, and other unknown effects. Blocking on runs significantly reduced the estimated pure error by over 50%. Blocking effects are observed when the variability transmitted from nuisance factors influence the experimental response, but in which we are not directly interested. A block consists of a data set of the measured variable in which the controlled variable is varied but the extraneous variable (in our case the tests performed between breaks or in different days and with different freestream conditions) is fixed. In the analysis of the tests all the data are combined. The results of each block will include each extraneous variable's influence as a variation. The data analysis produced functions of α, with estimates of the least significant difference (LSD) error for each response function to indicate the precision of the response models. The uncertainty in the predictions of each response model is attributable to multiple sources. The main error groups can be identified as follows:

1) Pure error: intrinsic random variation in the data points.

Table 1 Values of constant model parameters

Coeff. Eq. no.	n (4)	C_L (5)	C_D (6)	C_m (7)	C_L (8)-BR	C_D (9)-BR	C_m (10)-BR	C_L (8)-PR
a_0	−1.1050E − 01	2.4475E − 01	3.4812E − 02	−2.5413E − 01	6.8397E − 02	9.0514E − 02	−8.0310E − 02	6.8397E − 02
a_1	1.9200E − 02	−5.3300E − 03	5.6708E − 04	6.7541E − 03	−4.1313E − 04	−3.5769E − 04	2.1323E − 03	−4.1313E − 04
a_2	1.5000E − 02	−4.3240E − 03	6.1753E − 04	−5.9661E − 03	3.6876E − 02	−5.5657E − 03	−1.0160E − 02	3.6876E − 02
a_3	−4.0000E − 04	3.8150E − 02	−6.0652E − 03	−9.9239E − 03	1.5355E − 03	5.5510E − 04	5.1153E − 04	1.5355E − 03
a_4	3.4678E + 00	1.0679E − 04	5.3973E − 06	6.8781E − 05	8.2265E − 06	5.8847E − 04	−1.0353E + 00	8.2265E − 06
a_5	−9.0000E − 04	−5.7370E − 05	1.4502E − 04	−4.6192E − 05	2.3779E − 06	——	−1.2266E − 05	2.3779E − 06
a_6	−3.0000E − 04	3.5830E − 05	−1.1589E − 04	1.9610E − 04	2.2981E − 05	——	−3.7430E − 05	2.2981E − 05
a_7	3.0000E − 04	1.9583E − 04	−6.1578E − 06	−2.2674E − 06	1.0281E − 06	——	−5.8323E − 06	1.0281E − 06
a_8	−1.4500E − 01	2.7788E − 04	−6.6950E − 05	——	3.0348E − 04	——	5.1268E − 07	3.0348E − 04
a_9	——	7.0367E − 07	2.2509E − 04	——	−2.7006E − 05	——	——	−2.7006E − 05
a_{10}	——	3.1544E − 06	1.1342E − 06	——	——	——	——	——
a_{11}	——	4.7175E − 06	−1.0929E − 06	——	——	——	——	——
a_{12}	——	——	2.6460E − 06	——	——	——	——	——
a_{13}	——	——	1.6266E − 06	——	——	——	——	——
a_{14}	——	——	1.1618E − 05	——	——	——	——	——

Table 2 Values of constant model parameters

Coeff. Eq. no.	C_D (9)-PR	C_m (10)-PR	C_L (11)	C_L (12)	C_D (13)	C_m (14)	C_L (15)	C_D (16)
a_0	9.0514E − 02	−1.0669E − 01	1.0524E + 00	−6.3227E − 02	8.8137E − 01	−2.4632E − 01	−2.3623E + 01	−3.7158E + 01
a_1	−3.5769E − 04	2.7412E − 03	3.5739E − 04	7.0463E − 04	2.0199E − 04	−7.9879E − 04	2.3773E − 02	1.2970E − 02
a_2	−5.5657E − 03	−9.4347E − 03	4.8860E − 02	5.9292E − 02	−5.5996E − 03	−1.1822E − 02	2.1145E + 00	2.3235E + 00
a_3	5.5510E − 04	9.0136E − 04	−3.1638E − 01	−2.0990E − 03	8.1962E − 04	1.8272E − 02	−6.1469E − 02	4.5445E − 03
a_4	5.8847E − 04	−2.9626E − 01	−2.8758E − 05	1.5606E − 03	−8.8852E − 02	−4.3893E − 03	4.2466E − 02	1.3140E + 00
a_5	——	−1.6288E − 05	−8.7326E − 05	−9.7603E − 05	−4.6516E − 05	2.7862E − 05	3.4400E − 03	−7.1607E − 02
a_6	——	−3.5349E − 05	1.1735E − 03	−2.6900E − 05	1.2739E − 03	1.5116E − 05	6.1414E − 04	−4.1000E − 04
a_7	——	−3.5030E − 05	3.1178E − 04	3.1900E − 04	2.5972E − 03	——	−9.5791E − 04	7.5376E − 04
a_8	——	4.8973E − 07	2.3281E − 02	4.2722E − 05	−4.2488E − 02	——	1.7915E − 04	−3.6213E − 02
a_9	——	——	——	——	1.9689E − 05	——	−2.5470E − 05	——

2) Lack of fit: imperfections in the degree to which low-order polynomials represent the true (and unknown) underlying relationships.

3) Site selection: the uncertainty at a given angle of attack depends on how far that point is from the "center of mass" of points used to fit the models.

The range of angle of attack was divided for modeling purposes into two areas corresponding to the linear and nonlinear aerodynamics (with different boundary values for the cases with and without propeller). For the current work, the complete combinations of velocity and elevator deflection are available only for positive elevator deflection. The response surfaces for the three aerodynamic coefficients in the linear region of angle of attack (between 4 and 18 deg) for a vehicle equipped with a PR wing resulted in the following functions of α, q, and δ:

$$C_L = a_0 + a_1 q + a_2 \delta + a_3 \alpha + a_4 q\delta + a_5 \delta\alpha + a_6 q^2 + a_7 \delta^2 + a_8 \alpha^2 + a_9 q^2 \delta + a_{10} \delta^2 \alpha + a_{11} \delta^3 \tag{5}$$

$$C_D = a_0 + a_1 q + a_2 \delta + a_3 \alpha + a_4 a\delta + a_5 q\alpha + a_6 \delta\alpha + a_7 q^2 + a_8 \delta^2 + a_9 \alpha^2 + a_{10} q\delta\alpha + a_{11} q^2 \alpha + a_{12} \delta^2 \alpha + a_{13} \delta^3 + a_{14} \alpha^3 \tag{6}$$

$$C_m = a_0 + a_1 q + a_2 \delta + a_3 \alpha + a_4 q\delta + a_5 q^2 + a_6 \delta^2 + a_7 q\delta^2 \tag{7}$$

In the case of negative elevator angles, only two combinations of high–low elevator deflection and velocity are available. Therefore a two-level full factorial design was generated with α, q, and δ as factors. Such a design can quantify all three main effects, all three two-way interactions, and the one three-way interaction. Only eight data points are required, including all combinations of low and high α (4 and 18 deg), low and high q (corresponding to velocities of 10 and 13 m/s) and low and high elevator deflection δ (zero and full negative deflection). A null hypothesis is formed for all seven main effects and interactions and rejected only if the effect is large enough (compared to random error) to claim that it is nonzero with at least 95% confidence. To reject the null hypothesis in this test, effects must be sufficiently different from zero (positive or negative) such that there is no more than a 5% probability that this decision is made erroneously due to chance variations in the data. If the null hypothesis is not rejected, the effect may still be real, but simply too small to resolve with 95% confidence given the experimental error in the data.

When the effects can be considered too small to determine if they are real, we can resolve the problem by acquiring additional data to permit the random error to further cancel or by achieving a higher resolution by blocking some variables. The proposed procedure involved the use of only 8 data points as the high–low combinations of the three factors examined were blocked with respect to angle of attack. However, eight levels of angle of attack (factor C) with four combinations of high–low elevator deflection (factor B) and dynamic pressure (factor A) were available for a total of 32 data points. By establishing a two-level, two-factor experiment in the factors A and B, and replicating this at the eight levels of factor C by using factor C as a blocking variable, we can obtain a higher resolution of the A and B main effects and the AB interaction, at the relatively low cost of losing any information on whether α impacts the responses (a generally well-established dependency). Probability plots were used to scan the results, discerning true effects from random variations of the desired effectors. The main characteristic of these plots is that noise effects due to random error falls along a straight line, while true effects are displaced from the line. An example of the above technique is illustrated in Fig. 8, with the

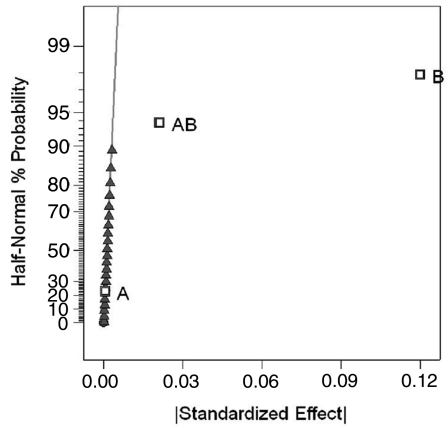

Fig. 8 Probability plot for C_L, without propeller.

coefficient of lift. The effect of A (dynamic pressure) is on the straight line and therefore can be considered irrelevant. However, the effect of B and AB (elevator deflection and dynamic pressure-elevator deflection interaction, respectively) are true effects. From similar plots for the other variables, several inferences can be made about the functional dependencies between independent variables and output responses, as summarized in Table 3.

The drag was influenced more by the dynamic pressure than the elevator deflection, but the opposite was true for lift and pitching moment. Elevator authority was influenced by dynamic pressure for lift, drag, and pitching moment, for both positive and negative elevator deflections. The plots seen in Fig. 9 demonstrate the interaction between elevator angle and dynamic pressure on the lift, drag, and pitching moment coefficients. It is evident that C_L decreases as the elevator angle decreases, but at a slightly higher rate for higher dynamic pressure. The two effects are similar, as confirmed by the probability plot in Fig. 8. There is a significant difference in the response of C_D with elevator angle for the two levels of dynamic pressure, demonstrating a dependency with the dynamic pressure only for lower levels of velocity. Figure 9 also reveals the interaction between elevator angle and dynamic pressure on the pitching moment coefficient. The pitching moment increases as the elevator goes more negative, but at a greater rate for higher dynamic pressure.

An attempt was made to determine the models in the complete range of elevator deflection angles in the linear region. To compensate for the lack of test runs with negative elevator angles, only the symmetric test runs in the subspaces of dynamic pressure and elevator deflection were used for the regression analysis. The results were less accurate with respect to the positive elevator deflection but still exhibited acceptable R^2 values between 0.954 and 0.998. The former value, attributed to the C_m, was the lowest yet observed. The resulting models for the BR wing are as follows:

Table 3 Summary of dependencies for the two-level, two-factor full factorial design

	Reject null hypothesis?		
Effect	C_L	C_D	C_m
A	**No**	Yes	Yes
B	Yes	Yes	Yes
AB	Yes	Yes	Yes

$$C_L = a_0 + a_1 q + a_2 \alpha + a_3 \delta + a_4 q\alpha + a_5 \delta\alpha + a_6 q\delta + a_7 \delta^2\alpha + a_8 \alpha^2 + a_9 \delta^2 + a_{10} \delta^3 \tag{8}$$

$$C_D = a_0 + a_1 q + a_2 \delta + a_3 \delta + a_4 \alpha^2 + a_5 \delta^2 + a_6 q\alpha + a_7 q\delta + a_8 \alpha\delta + a_9 q\alpha^2 + a_{10} \delta\alpha^2 \tag{9}$$

$$C_m = a_0 + a_1 q + a_2 \alpha + a_3 \delta + a_4 q\delta + a_5 q^2 + a_6 \delta^2 + a_7 \alpha^2 + a_8 q\delta^2 \tag{10}$$

The models from the comparable tests runs with the PR wing are characterized by the same model structure but different parameters, as reported in Tables 1 and 2. The models for the C_m of the two wings are similar, but the PR wing shows a significantly stronger coupling with the dynamic pressure and a moderate coupling with angle of attack, as expected. The elevator angle effects are similar for both wings.

D. Aerodynamic Coefficients with Propeller

The propeller-on experiments were carried out with an asymmetry of runs between positive and negative elevator deflection. The results included the total aerodynamic coefficients C_L, C_D, and C_m, combining the effects of the wing aerodynamics and the propeller forces. An example for lift is illustrated in Fig. 10. The database acquired during the propeller-on tests was used to estimate the models for the coefficients using two different methodologies. One procedure used the motor voltage input as an independent variable; the model for the lift coefficient was estimated in the linear regime for positive elevator angle deflections:

$$C_L = a_0 + a_1 q + a_2 \delta + a_3 \alpha + a_4 E + a_5 q\delta + a_6 q\alpha + a_7 \delta E + a_8 \alpha^2 + a_9 E^2 \tag{11}$$

The model is a second-order function of α and motor voltage, which reflects the nonlinear dependence of rpm on α and freestream velocity. The lift coefficient is directly proportional to dynamic pressure, with a slope that depends on α and motor voltage (thus the propeller speed). The plot seen in Fig. 11 illustrates how the motor voltage affects elevator authority. The p-stat for this dependence is <0.0001, meaning there is more than a 99.99% probability that the

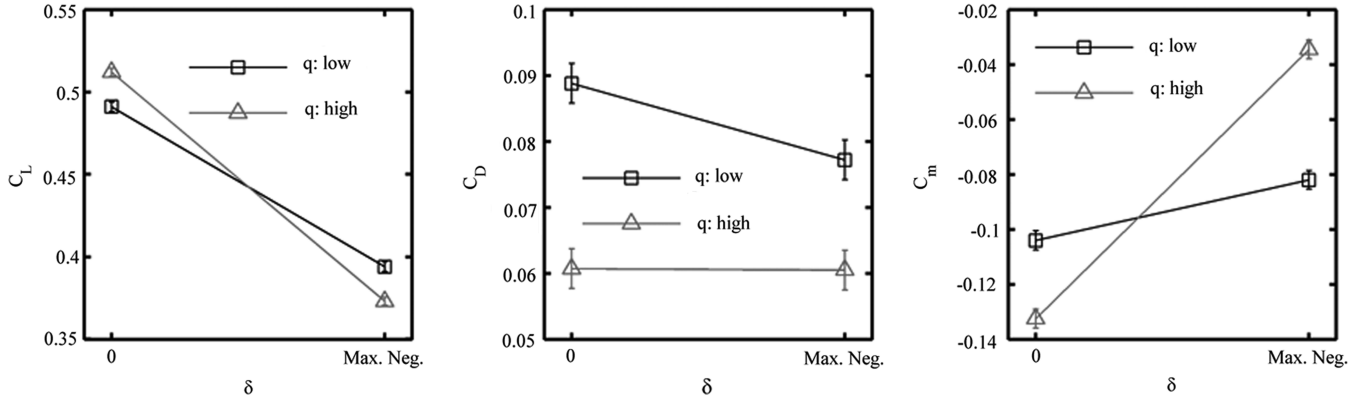

Fig. 9 Interaction plots for the aerodynamic coefficients with q as a parameter.

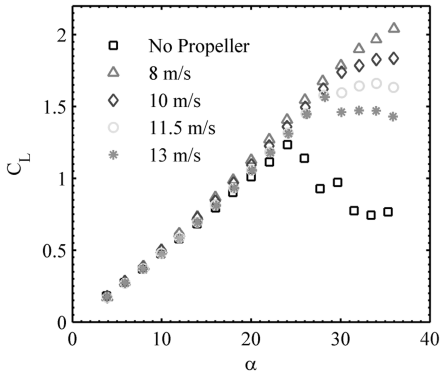

Fig. 10 Lift coefficients of a PR wing at four different freestream velocities and motor voltage of 7.4 V: the propeller-off condition is illustrated at 13 m/s for comparison.

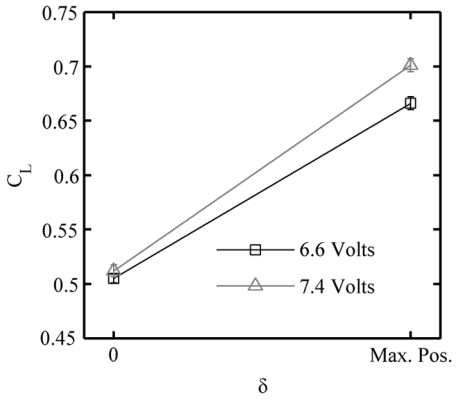

Fig. 11 Interaction plots for the lift coefficient with motor voltage as a parameter.

dependence is real. The lift increases with elevator deflection, but at zero deflection the lift at 6.6 V is indistinguishable from the lift at 7.4 V. However, at full deflection, higher voltage translates into higher lift, resulting in more elevator authority.

An alternative method used the functional dependence of propeller speed expressed by Eq. (5) instead of motor voltage. In this case the propeller speed was a pseudoindependent variable; the response surfaces of the coefficients contain terms in the propeller speed in krpm. For C_m the model could not produce a good fit in the nonlinear region. High scatter of the experimental data for negative elevator deflection angles and an intrinsic noise in the data for high α are possible causes of the model's poor predictive capability. The models for the response surfaces estimated with the aforementioned method are as follows. For the linear region of lift and for all elevator angle deflections (between -30 and $+30$ deg),

$$C_L = a_0 + a_1 q + a_2 \alpha + a_3 n + a_4 q\alpha + a_5 q\delta + a_6 n\delta + a_7 \alpha\delta \tag{12}$$

$$C_D = a_0 + a_1 q + a_2 \alpha + a_3 \alpha^2 + a_4 n + a_5 q\alpha + a_6 \delta + a_7 n^2 + a_8 n^2/q + a_9 \delta^2 \tag{13}$$

$$C_m = a_0 + a_1 q + a_2 \alpha + a_3 n + a_4 \delta + a_5 q\alpha + a_6 q\delta + a_7 n\delta + a_8 \alpha^4 \tag{14}$$

The above equations are plotted in Fig. 12 for three voltage settings. The linear relationship between angle of attack, elevator angle, and lift/pitching moment is clearly evident, as are the nonlinear drag dependencies. Higher motor voltage has a negligible effect upon the lift, but does noticeably change the drag and pitching moment. For the nonlinear region of lift and for all elevator angle deflections (between -30 and $+30$ deg),

$$C_L = a_0 + a_1 q + a_2 \alpha + a_3 \alpha^2 + a_4 n + a_5 \delta + a_6 \alpha^3 + a_7 q\alpha + a_8 \alpha\delta + a_9 q\delta \tag{15}$$

$$C_D = a_0 + a_1 q + a_2 \alpha + a_3 \delta + a_4 n + a_5 \alpha^2 + a_6 q\alpha + a_7 \alpha^3 + a_8 n^2 \tag{16}$$

V. Conclusions

Wind-tunnel experiments on a powered MAV with various flexible-wing designs and variable elevator deflections proved effective for obtaining the aerodynamic coefficients in forms of linear regression models and investigating the mutual dependencies between the variables. The variation of the regression models and variable responses with dynamic pressure and angle of attack due to the propeller speed and wing flexibility effects is demonstrated. The flexible-wing out-of-plane displacement field induced by the propeller slipstream was explored by measuring the difference between the port and starboard wing shape, demonstrating a geometric asymmetry. This asymmetric effect decreases at higher angles of attack and at higher dynamic pressure as it is overwhelmed by the symmetric deformation from the freestream aerodynamics.

The proposed propeller speed model contains a linear term with dynamic pressure and nonlinear terms with motor input voltage and angle of attack. The model of the lift coefficient resulted in a second-order function in the angle of attack and in motor voltage, which reflects the nonlinear dependence of the propeller speed on the angle of attack and freestream velocity. The lift coefficient is directly proportional to the dynamic pressure, with a slope that depends on angle of attack and motor voltage, thus the propeller speed. Results of the aerodynamic tests without propeller revealed that the dynamic pressure influenced the drag more than the elevator deflection, elucidating the flexible-wing shape deformation effects. The perimeter reinforced wing rate of change in lift coefficient is larger with respect to the batten reinforced wing as demonstrated from the higher lift-to-dynamic pressure and lift-to-angle-of-attack slopes. Elevator deflection was more influential than the dynamic pressure

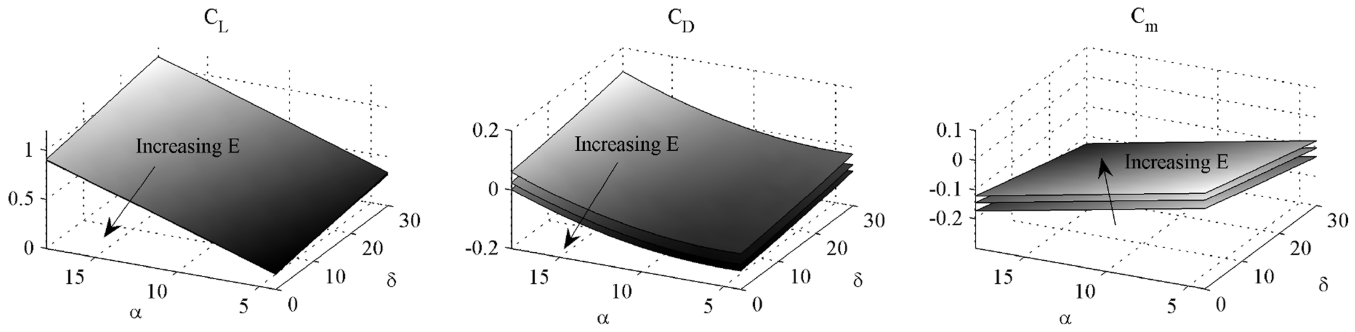

Fig. 12 Aerodynamic coefficient response surfaces for 6, 7, and 8 V of power.

for lift and pitching moment variation. Furthermore, elevator authority is influenced by dynamic pressure for lift, drag, and pitching moment for both positive and negative elevator deflections. The rate of change of the aerodynamics at different elevator angle is dynamic pressure dependent. For example, the pitching moment increases as elevator deflection becomes more negative, but at a greater rate for higher dynamic pressure.

Future work will consist of wind-tunnel measurements with six components in a series of tests with multiple controls (elevator, rudder, wing morphing). In addition, experiments will be conducted simulating the flight conditions with the angle of attack not equal to the pitch angle, by using a custom designed pitching–plunging mechanism.

Acknowledgments

This work was supported jointly by the U.S. Air Force Research Laboratory and the U.S. Air Force Office of Scientific Research under F49620-03-1-0381 with Todd Combs, Sharon Heise, and Johnny Evers as project monitors and by the Research Institute for Autonomous Precision-Guided Systems under F49620-1-0170 and FA9550-07-1-0236 with Fariba Fahroo as project monitor. The authors would also like to acknowledge the technical contributions and funding of Martin Waszak at the NASA Langley Research Center.

References

[1] Lian, Y., and Shyy, W., "Three Dimensional Fluid Structure Interactions of a Membrane Wing for MAV Applications," AIAA Paper 2003-1726, 2003.

[2] Viieru, D., Albertani, R., Shyy, W., and Ifju, P., "Effect of Tip Vortex on Wing Aerodynamics of Micro Air Vehicles," *Journal of Aircraft*, Vol. 42, No. 6, 2005, pp. 1530–1536.

[3] Torres, G. E., "Aerodynamics of Low Aspect Ratio Wings at Low Reynolds Numbers with Applications to Micro Air Vehicle Design," Ph.D. Dissertation, Department of Aerospace and Mechanical Engineering, University of Notre Dame, South Bend, IN, 2002.

[4] Pellettier, A., and Mueller, T., "Low Reynolds Number Aerodynamics of Low-Aspect Ratio, Thin/Flat/Cambered-Plate Wings," *Journal of Aircraft*, Vol. 37, No. 5, 2000, pp. 825–832.

[5] Waszak, M., Jenkins, L., and Ifju, P., "Stability and Control Properties of an Aeroelastic Fixed Wing Micro Aerial Vehicle," AIAA Paper 2001-4005, 2001.

[6] Albertani, R., Stanford, B., Hubner, J., and Ifju, P., "Aerodynamic Characterization and Deformation Measurements of a Flexible Wing Micro Air Vehicle," *Experimental Mechanics*, Vol. 47, No. 5, 2007, pp. 625–635. doi:10.1007/s11340-006-9025-5

[7] Albertani, R., Stanford, B., Hubner, J., and Ifju, P., "Characterization of Flexible Wing MAVs: Aeroelastic and Propulsion Effects on Flying Qualities," AIAA Paper 2005-6324, 2005.

[8] Waszak, M., Davidson, J., and Ifju, P., "Simulation and Flight Control of an Aeroelastic Fixed Wing MAV," AIAA Paper 2002-4875, 2002.

[9] Morelli, E., "Global Nonlinear Aerodynamic Modeling Using Multivariate Orthogonal Functions," *Journal of Aircraft*, Vol. 32, No. 2, 1995, pp. 270–277.

[10] DeLoach, R., "Applications of Modern Experiment Design to Wind Tunnel Testing at NASA Langley Research Center," AIAA Paper 98-0713, 1998.

[11] Albertani, R., "Experimental Aerodynamic and Elastic Deformation Characterization of Low Aspect Ratio Flexible Fixed Wings Applied to Micro Aerial Vehicles," Ph.D. Dissertation, Department of Mechanical and Aerospace Engineering, University of Florida, Gainesville, FL, 2005.

[12] Sutton, M., Turner, J., Bruck, H., and Chae, T., "Full Field Representation of the Discretely Sampled Surface Deformations for Displacement and Strain Analysis," *Experimental Mechanics*, Vol. 31, No. 2, 1991, pp. 168–177. doi:10.1007/BF02327571

[13] Morelli, E., and DeLoach, R., "Wind Tunnel Database Development Using Modern Experiment Design and Multivariate Orthogonal Functions," AIAA Paper 2003-0653, 2003.

[14] Montgomery, D., *Design and Analysis of Experiments*, 6th ed., Wiley, New York, 2005.

[15] Jenkins, D., Ifju, P., Abdulrahim, M., and Olipra, S., "Assessment of the Controllability of Micro Air Vehicles," *16th Bristol International RPV/UAV Conference*, 3–5 April 2001.

[16] Prandtl, L., "Mutual Influence of Wings and Propeller," Extract from *The First of the Gottingen Aerodynamic Laboratory*, Chap. IV, Sec. 6, NACA TN 74, Dec. 1921.